



#### RESEARCH PAPER •

Acta Mech. Sin., Vol. 39, 122393 (2023) https://doi.org/10.1007/s10409-022-22393-x

### A physically-based constitutive model for the prediction of yield strength in the precipitate-hardened high-entropy alloys

Siwei Ren<sup>1</sup>, Jia Li<sup>1</sup>, Hui Feng<sup>1\*</sup>, Peter K. Liaw<sup>2</sup>, and Qihong Fang<sup>1</sup>

<sup>1</sup> College of Mechanical and Vehicle Engineering, Hunan University, Changsha 410082, China; <sup>2</sup> Department of Materials Science and Engineering, The University of Tennessee, Knoxville, TN 37996, USA

Received November 9, 2022; accepted November 18, 2022; published online January 12, 2023

Precipitate-hardened high-entropy alloys (HEAs) exhibit great mechanical strength and exceptional ductility. However, the existing model fails to accurately predict the yield strength contributing from the solid solution strengthening and precipitate strengthening in the HEAs due to the neglect of the crucial roles including the complex chemical element, precipitate-size distribution, and the precipitate-spatial distribution. Moreover, a unified strength model for analyzing the yield strength in the HEAs is still lacking. A developed precipitate strengthening model considering the size distribution and spatial distribution is established and shows a higher accuracy compared to the existing model. The results show that the precipitate strengthening is the dominant contribution to the yield strength. It reveals that the effect of spatial distribution on precipitate strengthening is more pronounced than that of the precipitate-size distribution. This developed model provides a theoretical framework for determining the precipitate strengthening and the yield strength of HEA, and then subsequently guides the design of the high-strength HEAs.

High-entropy alloy, Precipitate strengthening, Size distribution, Spatial distribution, Strengthening model

Citation: S. Ren, J. Li, H. Feng, P. K. Liaw, and Q. Fang, A physically-based constitutive model for the prediction of yield strength in the precipitate-hardened high-entropy alloys, Acta Mech. Sin. 39, 122393 (2023), https://doi.org/10.1007/s10409-022-22393-x

#### 1. Introduction

High-entropy alloys (HEAs) have attracted significant attention in the past decades due to their great strength, superior structural stability, and corrosion resistance [1-5]. Unlike traditional alloys, HEAs generally comprise five or more elements with nearly equal atomic ratios [4,5]. Thus, the simple solid solution structures, such as the face-centered-cubic (FCC) structure and the body-centered-cubic (BCC) structure, are formed due to the high resultant configurational entropy [4,5]. The BCC HEAs have high strength and low elongation [6,7], while the FCC HEAs have good elongation and relatively low strength [8,9]. Among the HEAs, the FeCoCrNiMn HEA has the considerable tensile strength above 1 GPa and ductility of nearly 70% [4,10]. To obtain a better mechanical property,

the FeCoCrNiMn HEA has made modifications by changing the composition ratio and element kind. Some theoretical models have been developed for the analysis of the crystal plasticity and self-sharpening penetration [11,12].

The addition of Ti and Al elements in FeCoNi-based and FeCoCrNi-based HEAs improves the yield strength due to the formation of the spherical precipitates in the matrix [13-15]. Thus, the precipitate strengthening plays a key role in enhancing the mechanical properties of HEAs [16-18]. The precipitate strengthening is widely used in many alloys, such as Ni alloys [19], Al alloys [20], Mg alloys [21], and steels [22]. Recently, the precipitates to enhance the strength and ductility of the materials at the atomic level in FCC Cu with nanoprecipitates are studied using molecular dynamics simulations [23]. The results reveal that nanoprecipitates provide a unique type of dislocation source activated at sufficiently high-stress levels for increasing uniform plasticity [23]. Although the work about strengthening mechanisms has

<sup>\*</sup>Corresponding author. E-mail address: fenghuiff@hnu.edu.cn (Hui Feng) Executive Editor: Xiaoyan Li

been clearly explained, the quantitative prediction of strength contribution using the strengthening model is still lacking in HEAs due to the extremely complex chemical composition. The existing precipitate strengthening model developed is only to describe the simplified interactions between the dislocation and precipitate in the traditional alloys. The shearing mechanism and Orowan bypassing mechanism have been widely used in the precipitate strengthened alloys [24]. However, the existing models do not take into account the precipitate-size and -spatial distributions and the extremely atomic complex chemical composition in the novel HEA, and thus the unreasonable assessment of the solid solution and precipitate strengthening is a frequent occurrence.

Hence, a solid solution and precipitate strengthening model in the precipitate-hardened HEA is developed, to describe the strengthening contribution considering the effect of the precipitate-size and -spatial distributions and heterogeneous lattice distortion originating in the complex chemical composition. Here, instead of a single precipitate radius, a normal distribution of precipitates is considered. The Orowan bypassing mechanism is triggered when a dislocation passes through the large-radius precipitate. The triggered mechanism is the shearing mechanism when the dislocation passes through the small-radius precipitate. Besides, the existing strength models for predicting the strength in the precipitate-hardened HEA are inaccurate and do not give a detailed contribution from each strengthening mechanism. In the present work, we have coupled precipitate strengthening with solid solution strengthening, grain boundary strengthening, and dislocation strengthening to form a physically-based constitutive model for analyzing the yield strength of precipitate-hardened HEA. This model can analyze the contribution of each strengthening mechanism to yield strength. The effect of size and spatial distribution on precipitate strengthening is analyzed and discussed. Moreover, the findings obtained provide theoretical guidance for the preparation of high-strength HEAs by turning the precipitate size and fraction.

### 2. Precipitate strengthening

#### 2.1 Classical precipitate strengthening

Orowan bypassing and shearing mechanisms are the main strengthening mechanisms in precipitate strengthening. Of the two mechanisms, the one with a small value of precipitate strengthening is the operative mechanism.

When dislocations bypass the precipitates, they leave the dislocation loops, resulting in the precipitate strengthening. The Orowan bypassing strengthening can be calculated by the following formula [25,26]:

$$\sigma_{\text{Orowan}} = M \frac{0.4Gb}{\pi \sqrt{1 - \nu}} \frac{\ln(2\bar{r}/b)}{L_{\text{n}}},\tag{1}$$

where M is the Taylor factor; G is the shear modulus of the alloy; b is the Burgers vector; v is the Poisson ratio;  $\overline{r}$  is the mean precipitate radius on the slip planes, which can be written by  $\overline{r} = \sqrt{2/3} \cdot r$ , where r is the precipitate radius;  $L_{\rm p}$  is the mean interparticle spacing, and it can be calculated as  $L_{\rm p} = 2\overline{r} \left[ \sqrt{\pi/(4f)} - 1 \right]$ , where f is the precipitate volume fraction

When the dislocations shear the precipitates, three factors should be considered: the coherency strengthening ( $\sigma_{CS}$ ), the modulus mismatch strengthening ( $\sigma_{MS}$ ), and the order strengthening ( $\sigma_{OS}$ ). The three strengthening behaviors together constitute the shearing strengthening mechanism. The relevant expressions are as follows [27-29]:

$$\sigma_{\rm CS} = M \cdot \alpha_{\rm e} (G \cdot \varepsilon_{\rm I})^{3/2} [rf/(0.5Gb)]^{1/2}, \tag{2}$$

$$\sigma_{\rm MS} = 0.0055M(\Delta G)^{3/2} (2f/G)^{1/2} (r/b)^{3m/2-1},\tag{3}$$

$$\sigma_{\text{OS}} = 0.81 M \gamma_{\text{APB}} / (2b) \cdot (3\pi f / 8)^{1/2},$$
 (4)

$$\sigma_{\text{Shear}} = \sigma_{\text{CS}} + \sigma_{\text{MS}} + \sigma_{\text{OS}},\tag{5}$$

where  $\alpha_{\varepsilon}=2.6$  for the FCC structure; m=0.85;  $\varepsilon_{\rm L}$  is the constrained lattice parameter mismatch, which can be written by  $\varepsilon_{\rm L}=\frac{2}{3}\Delta a/a$ , where  $\Delta a$  is the constant lattice difference between precipitates and the FCC matrix, and  $\Delta a/a=0.0026$  [13];  $\Delta G$  is the shear modulus difference between the precipitate (77 GPa) adopted from Ni<sub>3</sub>(Al, Ti) and FeCoNiCr HEA (78.5 GPa) [13], and  $\Delta G=\left|G_{\rm HEA}-G_{\rm Precipitate}\right|$ ;  $\gamma_{\rm APB}$  is the anti-phase boundary (APB) energy of the precipitates.

Thus the curves of precipitate strengthening for the fixed precipitate volume fraction, and precipitate radius as the independent variable can be obtained in Fig. 1.

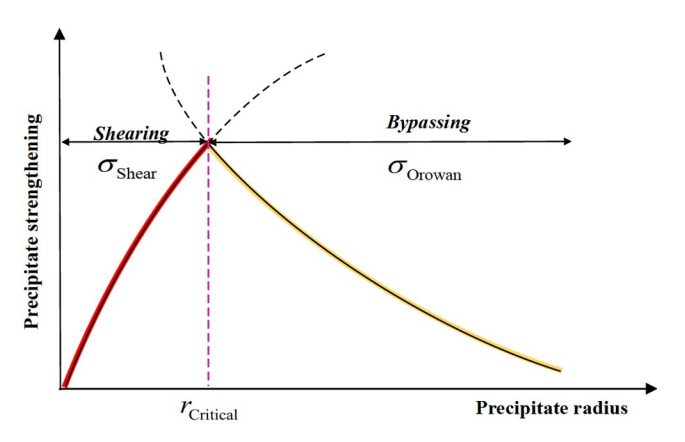


Figure 1 Corresponding precipitate strengthening mechanism under different precipitate radii.

As shown in Fig. 1, the curves of  $\sigma_{\rm Shear}$  and  $\sigma_{\rm Orowan}$  are interlaced. There is an important intersection  $r_{\rm Critical}$ .  $r_{\rm Critical}$  is the critical precipitate radius of the transition from the shearing mechanism to the Orowan bypassing mechanism. Thus the precipitate strengthening  $\sigma_{\rm PS}$  as a function of the precipitate radius can be summarized as follows:

$$\sigma_{\rm PS} = \begin{cases} \sigma_{\rm Shear}, & r \le r_{\rm Critical}, \\ \sigma_{\rm Orowan}, & r > r_{\rm Critical}. \end{cases}$$
 (6)

#### 2.2 Spatial distribution-dependent precipitate strengthening

Many experiments show that the precipitate shape in the HEAs is mostly spherical [13,15,30,31]. When dislocations move in the matrix, dislocations may interact with spherical precipitates at any position, so the actual shape of a single precipitate in the matrix should be considered. That is to say, considering the spatial distribution of precipitates. As shown in Fig. 2a, the dislocation slip plane in the spherical precipitate may not necessarily pass through the spherical center. The slip plane may shear or bypass the precipitate in either direction. Furthermore, Fig. 2b shows the triggering mechanism for precipitate strengthening when the precipitate is sheared or bypassed by dislocations through different cross sections. The active mechanism depends on whether r is greater or less than  $r_{\text{Critical}}$ .

The differential quadrature method calculates the precipitate strengthening controlled by different mechanisms. As shown in Fig. 2c, the precipitate radius h (h = r) is divided into two parts of OA and AB, the two parts are divided into n portions, respectively. According to continuum theory and calculus, n tends to positive infinity.  $h_{i+1} = h_i + dh$  (i = 1, 2, ..., n) in AB, where dh = AB/n, and  $h_{j+1} = h_j + dh$  (j = 1, 2, ..., n) in OA, where dh = OA/n. Thus Eqs. (1)-(5) can be rewritten as

$$\begin{aligned}
&\sigma_{\text{CS}}^{\text{Spatial}} = \frac{1}{n} \sum_{i=1}^{n} \sigma_{\text{CS}}(r_i), & r_i \leq r_{\text{Critical}}, \\
&\sigma_{\text{MS}}^{\text{Spatial}} = \frac{1}{n} \sum_{i=1}^{n} \sigma_{\text{MS}}(r_i), & r_i \leq r_{\text{Critical}}, \\
&\sigma_{\text{OS}}^{\text{Spatial}} = \sigma_{\text{OS}}, & r_i \leq r_{\text{Critical}}, \\
&\sigma_{\text{Shear}}^{\text{Spatial}} = \sigma_{\text{CS}}^{\text{Spatial}} + \sigma_{\text{MS}}^{\text{Spatial}} + \sigma_{\text{OS}}^{\text{Spatial}}, & r_i \leq r_{\text{Critical}}, \\
&\sigma_{\text{Orowan}}^{\text{Spatial}} = \frac{1}{n} \sum_{i=1}^{n} \sigma_{\text{Orowan}}(r_i), & r_i > r_{\text{Critical}}, \end{aligned} \tag{7}$$

for  $\sigma_{\mathrm{CS}}^{\mathrm{Spatial}}$  and  $\sigma_{\mathrm{MS}}^{\mathrm{Spatial}}$ ,  $r_i = \sqrt{r^2 - \left(r - h_i\right)^2}$ . However, based on Eq. (4), the precipitate radius is not essential for the value of  $\sigma_{\mathrm{OS}}^{\mathrm{Spatial}}$ , as  $\sigma_{\mathrm{OS}}^{\mathrm{Spatial}}$  is not influenced by the precipitate radius. As for  $\sigma_{\mathrm{Orowan}}^{\mathrm{Spatial}}$ ,  $r_j = \sqrt{r^2 - h_j^2}$ .

According to Fig. 2c, by differentiating the precipitate radius, the probabilities of the two mechanisms can be calculated. In the active region of the shearing mechanism  $(r \le r_{\text{Critical}})$ , the probability is equal to the ratio between the line AB and the precipitate radius. Therefore, the probability in the shearing mechanism region (AB region) can be calculated as

$$p_1 = \frac{AB}{r} = 1 - \sqrt{1 - \left(\frac{r_{\text{Critical}}}{r}\right)^2}.$$
 (8)

For the Orowan bypassing mechanism region (*OA* region), the probability can be calculated as

$$p_2 = 1 - p_1. (9)$$

Combined Eqs. (6)-(9), the precipitate strengthening considering spatial distribution ( $\sigma_{PS}^{Spatial}$ ) under different precipitate radii can be obtained by

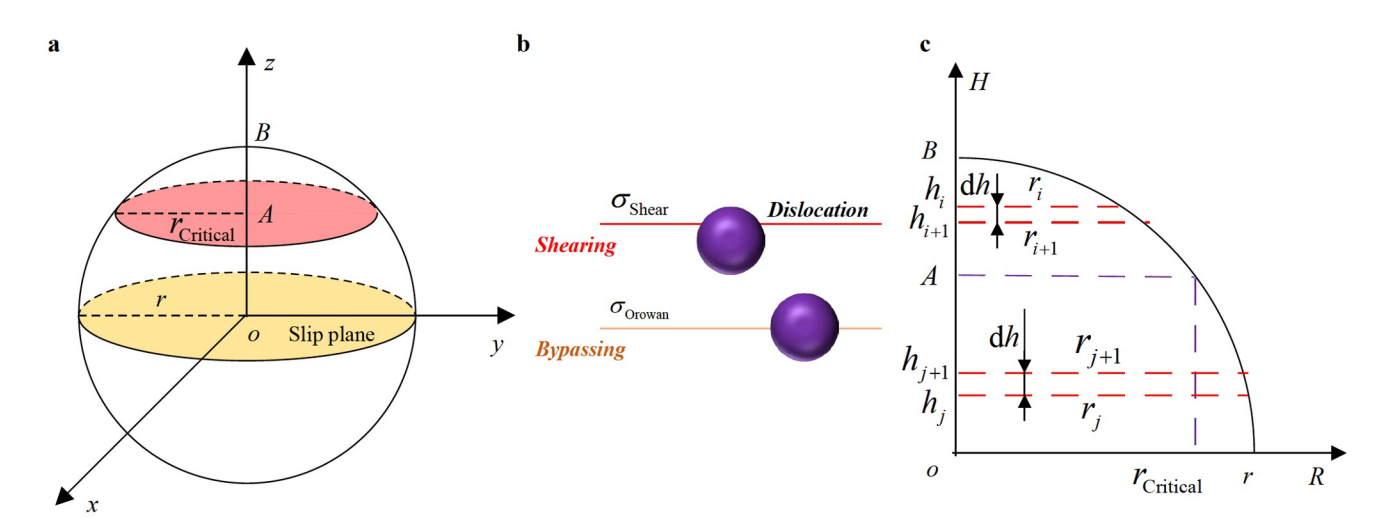


Figure 2 Schematic diagram of the dislocation bypassing a precipitate. a Spherical precipitate; b dislocation shearing or bypassing the precipitate; c differentiating the precipitate radius.

$$\begin{cases}
\sigma_{\text{PS}}^{\text{Spatial}} = \sigma_{\text{Shear}}^{\text{Spatial}}, & r \leq r_{\text{Critical}}, \\
\sigma_{\text{PS}}^{\text{Spatial}} = p_1 \cdot \sigma_{\text{Shear}}^{\text{Spatial}} + p_2 \cdot \sigma_{\text{Orowan}}^{\text{Spatial}}, & r > r_{\text{Critical}}.
\end{cases}$$
(10)

# 2.3 Size distribution-dependent precipitate strengthening

As shown in Fig. 3, the precipitate-size distribution in the FeCoCrNiTiAl HEA is approximately normal distribution [32]. The probability density can be expressed as

$$f_{\rm p}(r) = \frac{1}{\sqrt{2\pi}\sigma} \exp\left[-\frac{(r - r_{\rm Ave})^2}{2\sigma^2}\right],\tag{11}$$

where  $\sigma$  is the standard deviation, and  $r_{\text{Ave}}$  is the average radius of precipitates.

When the average radius of precipitates meets  $r_{\text{Ave}} > r_{\text{Critical}}$ , the size distribution consists of two regions. It includes the shearing mechanism region ( $r \le r_{\text{Critical}}$ ), and the Orowan bypassing mechanism region ( $r > r_{\text{Critical}}$ ) (Fig. 4a). As shown in Fig. 4b, according to the infinitesimal method, the precipitate radius in each mechanism region is divided into n portions (n tends to positive infinity). The precipitate strengthening contribution of the corresponding part is equal to the product of the probability of the precipitate radius and the corresponding precipitate strengthening. The contributed precipitate strengthening from the mechanism region is the sum of the contribution of precipitate strengthening in the corresponding n portions.

The size distribution-dependent precipitate strengthening considers spatial distribution in two regions and can be

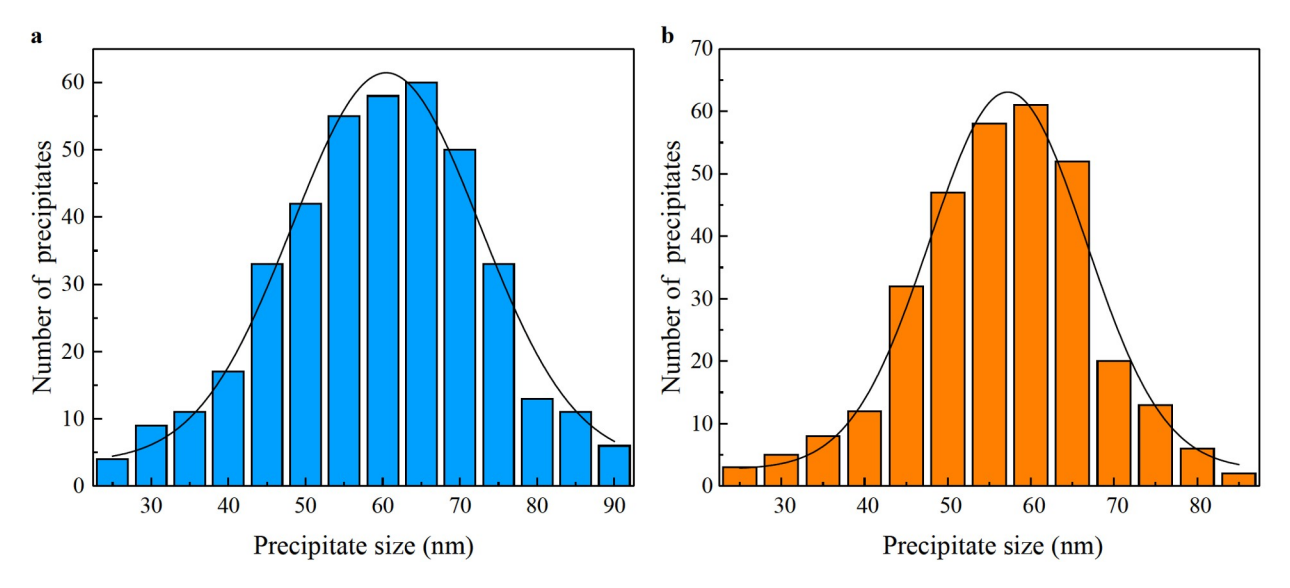


**Figure 3** Precipitate size distribution. **a** Aged solution treated and 25% pre-deformed sample conditions at an aging time of 240 h and the temperature of 1023 K in the FeCoCrNiTiAl HEA [32]; **b** solution-treated sample conditions at an aging time of 240 h and the temperature of 1023 K in the FeCoCrNiTiAl HEA [32].

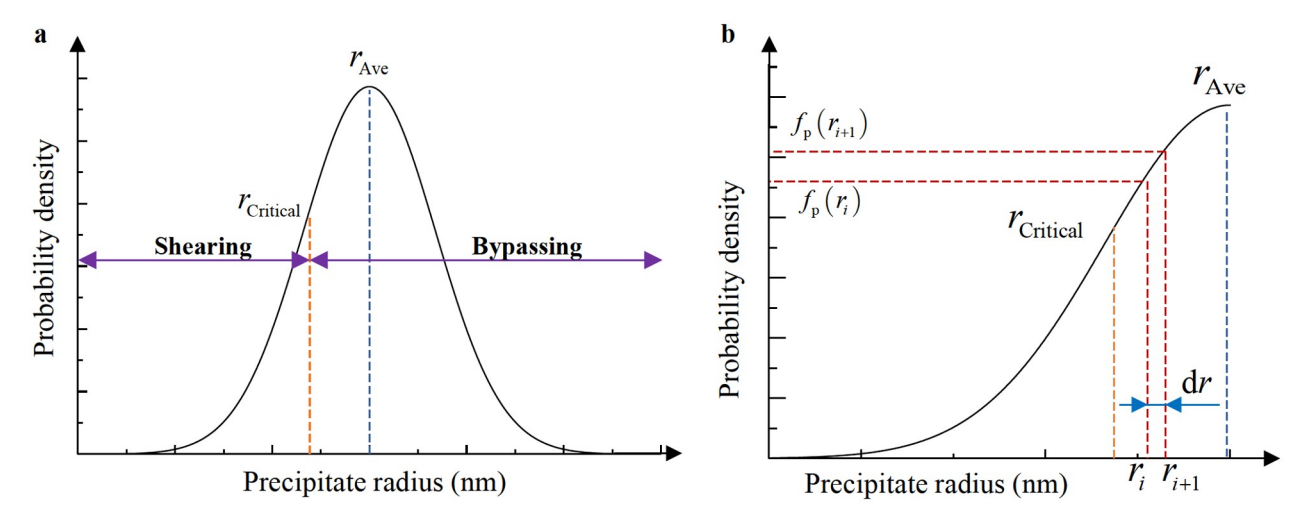


Figure 4 a Normal distribution diagram of the precipitate size; b schematic diagram for calculating the contributed precipitate strengthening by the infinitesimal method.

expressed as

$$\begin{cases}
\sigma_{\text{CS}}^{\text{Size}} = \sum_{i=1}^{n} \sigma_{\text{CS}}^{\text{Spatial}}(r_{i}) \int_{r_{i}}^{r_{i+1}} f_{p}(r) \, dr, & r \leq r_{\text{Critical}}, \\
\sigma_{\text{MS}}^{\text{Size}} = \sum_{i=1}^{n} \sigma_{\text{MS}}^{\text{Spatial}}(r_{i}) \int_{r_{i}}^{r_{i+1}} f_{p}(r) \, dr, & r \leq r_{\text{Critical}}, \\
\sigma_{\text{OS}}^{\text{Size}} = \sum_{i=1}^{n} \sigma_{\text{OS}}^{\text{Spatial}} \int_{r_{i}}^{r_{i+1}} f_{p}(r) \, dr, & r \leq r_{\text{Critical}}, \\
\sigma_{\text{Shear}}^{\text{Size}} = \sigma_{\text{CS}}^{\text{Size}} + \sigma_{\text{MS}}^{\text{Size}} + \sigma_{\text{OS}}^{\text{Size}}, & r \leq r_{\text{Critical}}, \\
\sigma_{\text{Orowan}}^{\text{Size}} = \sum_{i=1}^{n} \sigma_{\text{Orowan}}^{\text{Spatial}}(r_{i}) \int_{r_{i}}^{r_{i+1}} f_{p}(r) \, dr, & r > r_{\text{Critical}},
\end{cases}$$

$$(12)$$

where  $\sigma_{\mathrm{Shear}}^{\mathrm{Size}}$  is the sum of the precipitate strengthening contributed by each portion in the shearing mechanism region  $(r \leq r_{\mathrm{Critical}})$ ,  $\sigma_{\mathrm{Orowan}}^{\mathrm{Size}}$  represents the sum of the precipitate strengthening contributed by each portion in the Orowan bypassing mechanism region  $(r > r_{\mathrm{Critical}})$ .

Hence, based on the size distribution and spatial distribution of the precipitates, the new precipitate strengthening model is expressed as

$$\sigma_{\rm PS}^{\rm New} = \sigma_{\rm Shear}^{\rm Size} + \sigma_{\rm Orowan}^{\rm Size}.$$
 (13)

#### 2.4 Yield strength

The yield strength  $\sigma_{\rm YS}$  in the precipitate-hardened HEAs comes from the contribution of four strengthening mechanisms, including the solid solution strengthening  $\sigma_{\rm SS}$ , grain boundary strengthening  $\sigma_{\rm GB}$ , dislocation strengthening  $\sigma_{\rm Dis}$ , and precipitate strengthening  $\sigma_{\rm PS}$ . Therefore, the yield strength in precipitate-hardened HEAs is expressed as

$$\sigma_{\rm YS} = \sigma_{\rm SS} + \sigma_{\rm GB} + \sigma_{\rm Dis} + \sigma_{\rm PS}. \tag{14}$$

The elastic mismatch and atomic size mismatch of the HEA matrix lead to the lattice distortion. Based on the previous work [33], the solid solution strengthening in the HEAs is calculated by the following equation:

$$\sigma_{\rm SS} = \sum_{i}^{n} AGc_{i}^{5/3} \delta p_{i}^{4/3}, \tag{15}$$

where A is a treatment processing-dependent and material-dependent non-dimensional constant,  $c_i$  is the concentration of the element i in the HEA, and  $\delta p_i$  is the mismatch parameter. Appendix A gives the detailed derivation process for the modified solid solution strengthening, and Appendix B provides the process for the classical solid solution strengthening.

Based on the Hall-Petch relationship, the grain boundary strengthening is expressed as [34,35]

$$\sigma_{\rm GB} = k_{\rm HP} / d_{\rm g},\tag{16}$$

where  $k_{\rm HP}$  is the Hall-Petch constant, and  $d_{\rm g}$  is the mean

grain size.

The dislocations interact with themselves and impede their movement. Therefore, the high dislocation density in the alloys results in the strong dislocation strengthening [36]. Based on the Bailey-Hirsch relationship [37], the dislocation strengthening is calculated as

$$\sigma_{\rm Dis} = M\alpha G b \sqrt{\rho} \,, \tag{17}$$

where  $\alpha$  is the empirical constant [15], and  $\rho$  is the dislocation density. The dislocation density at different strains is calculated through the constitutive model in Appendix C [38,39].

#### 3. Results and discussion

## 3.1 Validity of developed model and contribution of strengthening mechanism

The FeCoCrNiTiAl and FeCoNiTiAl HEAs obtained by different treatment processing (Details are given in Appendix D) [13-15] are analyzed to verify the accuracy of the developed model, and the yield strength calculated from our model is compared with the experiment and classical model. Table 1 shows the parameters used for calculating the strength of the HEAs. The shear modulus and atomic radius of the elements in the FeCoCrNiTiAl and FeCoNiTiAl HEAs are listed in Table D1 of Appendix D. The specimens of the FeCoCrNiTiAl HEA with various treatment processing are designated as TP1, TP2, and TP3, respectively. The specimens of FeCoNiTiAl HEA with various treatment processing are designated as T1, T2, and T3, respectively. The treatment processing and atomic fraction of TP1/TP2/ TP3 and T1/T2/T3 are listed in Tables D2 and D3 of Appendix D, respectively. Moreover, the constant A, dislocation density, grain size, precipitate radius, and volume fraction in FeCoCrNiTiAl and FeCoNiTiAl HEAs are listed in Table D4 of Appendix D.

Based on the experiments, the yield strength of the Fe-CoCrNiTiAl and FeCoNiTiAl HEAs is obtained through the classical model I, classical model II and the present model. Here, the classical model I is based on the classical solid

**Table 1** Parameters used in the present model for the HEA

Parameter	Symbol	Magnitude
Taylor factor	M	3.06
Burgers vector (nm)	b	0.255 [40]
Shear modulus difference (GPa)	$\Delta G$	1.5
Poisson ratio	ν	0.31 [14]
APB energy (J/m <sup>2</sup> )	$\gamma_{APB}$	0.12 [41]
Standard deviation	σ	3.4
Hall-Petch constant (MPa μm <sup>1/2</sup> )	$k_{ m HP}$	266 [35]
Empirical constant	$\alpha$	0.2 [15]

solution strengthening model and classical precipitate strengthening model; the classical model II is based on the modified solid solution strengthening model and classical precipitate strengthening model; the present model is based on the modified solid solution model and developed precipitate strengthening model. The strength from the rest of the strengthening mechanism is computed using the same model. As shown in Fig. 5, the error between the present model and the experiment is minor compared with the classical models I and II. The results calculated with the classical model I usually have a large deviation. Take TP2 alloy as an example, the yield strength of TP2 is 648 MPa, the yield strength calculated by the classical model I is 810.5 MPa, and the error is 25.1%. The yield strength calculated by the classical model II is 707.9 MPa, and the error is 9.3%. The yield strength calculated by the present model is 677.3 MPa, and the error is 4.5%. In contrast, the accuracy of our model is 20.6% higher than that of the classical model I and 4.7% higher than that of classical model II in TP2. Moreover, the calculation error of the present model is less than 10%, and the calculation accuracy is improved compared with the classical models I and II.

The contributions of various strengthening mechanisms on the yield strength in the FeCoCrNiTiAl and FeCoNiTiAl HEAs are presented in Fig. 6. Because the dislocation strengthening in TP1 and T1 calculated by the constitutive model in Appendix C are too small, they are ignored. From Fig. 6a, precipitate strengthening is dominant in the increment of the yield strength and contributes more than 50% of the strength. The highest contribution of precipitate strengthening reaches 87% (Fig. 6b). Although the precipitate radius and volume fraction in TP1 and TP2 are different, their treatment processes are almost the same (The treatment processing of TP1/2 is listed in Table D2 of Appendix D). There is nearly no difference in the precipitate strengthening and yield strength. However, compared with TP2, TP3 has a higher yield strength due to the contribution of dislocation strengthening. The dislocation strengthening accounts for 27% of the yield strength in TP3. This trend is consistent with the previous experimental result [42]. When the dislocation density is very high, the heterogeneous nucleation is dominant [42]. The massive nucleation increases the number of precipitates, resulting in the strong precipitate strengthening.

From Fig. 6c, precipitate strengthening plays a vital role in the yield strength, and the contribution of precipitate strengthening to yield strength is higher than 43%. Its highest contribution reaches 81% (Fig. 6d). Similar to the case in the FeCoCrNiTiAl HEA, compared with T1 and T2, T3 has high dislocation density. This trend makes the effect of dislocation strengthening obvious, and the contribution of dislocation strengthening accounts for up to 29% (Fig. 6d).

Based on the theoretical modeling results, there is no apparent competition between grain boundary strengthening and precipitate strengthening (Fig. 6a and c). Hence, the optimal choice is to reduce the grain size to increase the grain boundary strengthening. The increased dislocation density enhances the dislocation strengthening by adjusting the treatment processing, thereby improving the yield strength of the precipitate-hardened HEAs.

## 3.2 Effect of size distribution and spatial distribution on precipitate strengthening

To determine the influence of size distribution and spatial distribution on precipitate strengthening, the relationship between precipitate strengthening and precipitate radius is analyzed. Figure 7a shows the apparent differences between the present precipitate strengthening model and the classical precipitate strengthening model. When the precipitate radius meets  $r = r_{\text{Critical}}$ , the difference between the classical model and the present model is close to 100 MPa. The radius corresponding to the maximum precipitate strengthening is increased after considering the size and spatial distributions. Besides, the difference of the precipitate strengthening from the present and classical models becomes more prominent in

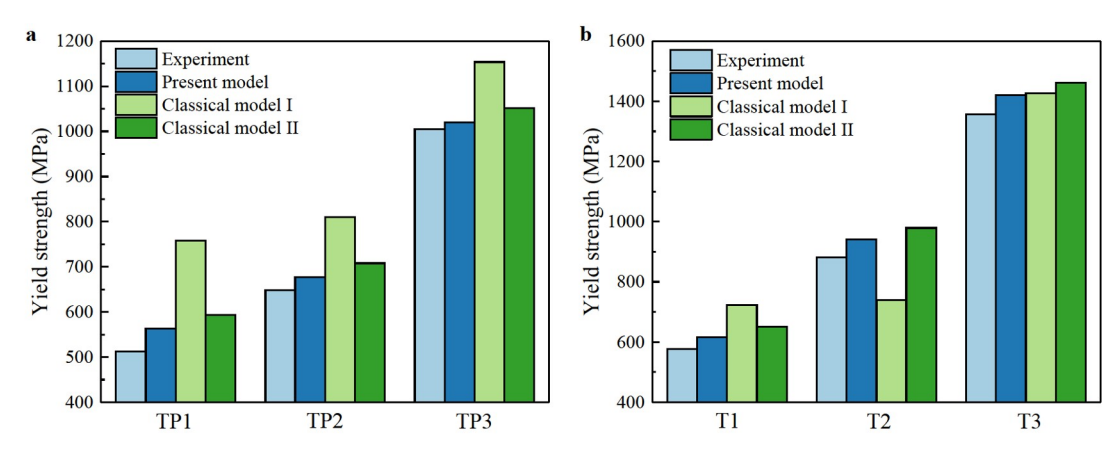


Figure 5 Comparison of yield strength from the experiments, classical models, and present model. a FeCoCrNiTiAl HEA; b FeCoNiTiAl HEA.

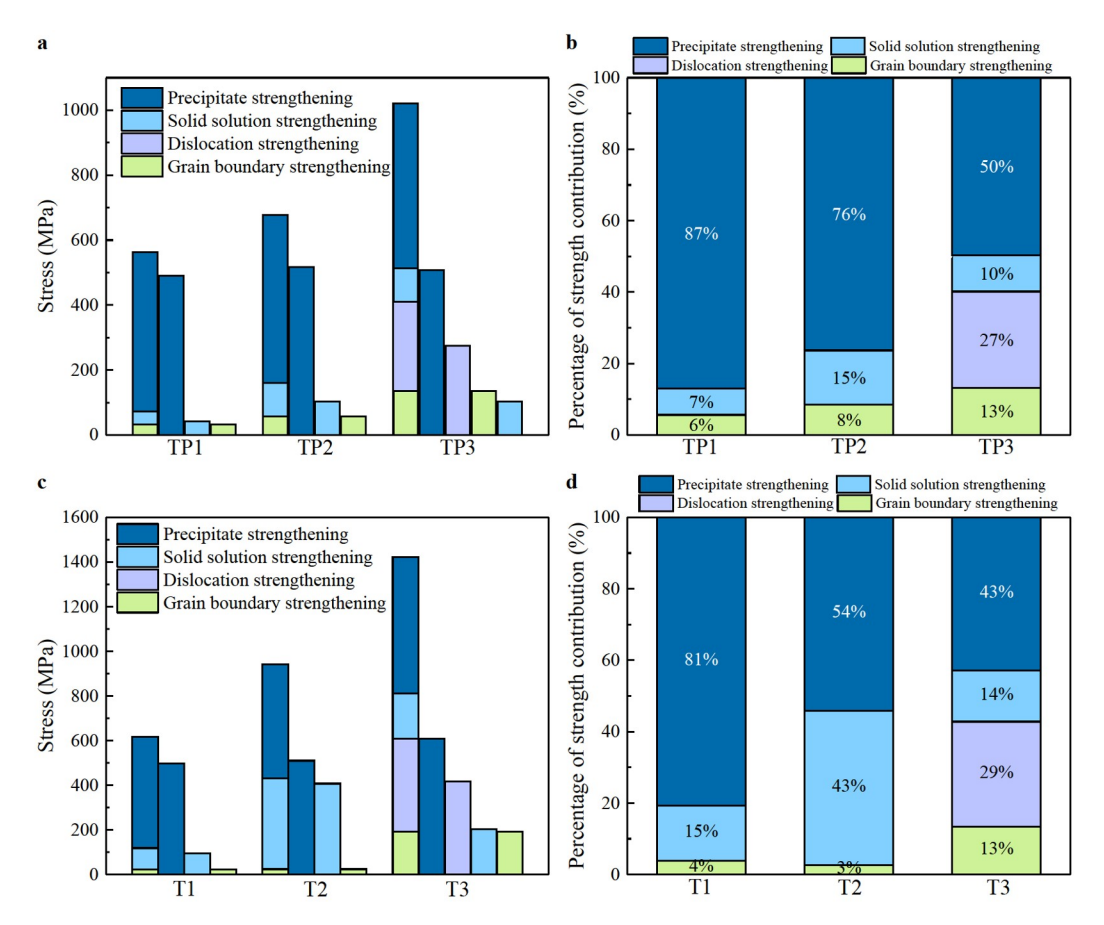


Figure 6 a Contribution of different strengthening mechanisms in the FeCoCrNiTiAl HEA; **b** yield strength from different strengthening mechanisms in the FeCoCrNiTiAl HEA; **d** yield strength from different strengthening mechanisms in the FeCoNiTiAl HEA; **d** yield strength from different strengthening mechanisms in the FeCoCrNiTiAl HEA.

the case of r > 50 nm, due to the contribution of the shearing mechanism considered in the developed model. According to Fig. 7b, the effect of the size distribution on precipitate strengthening is small, and the calculated value is almost no different from the classical model. The difference is only apparent when the precipitate radius is near the critical radius, and the difference between the classical model and the size distribution-dependent model is about 50 MPa.

Figure 7c reveals that the spatial distribution plays a critical role in the present model. With the increasing precipitate radius, the difference between the spatial distribution model and the classical model gradually obvious until it approaches  $r_{\text{Critical}}$ . The radius corresponding to the maximum precipitate strengthening of the spatial distribution model increases compared with the classical model. When the precipitate radius is slightly larger than the critical radius, the shearing mechanism and the Orowan bypassing mechanism can still enhance the precipitate strengthening. However, as the precipitate radius continues to increase, the proportion of the shear mechanism reduces, and the strength from the Orowan bypassing mechanism is insufficient to compensate for the strength loss caused by the reduction of the proportion of the shearing mechanism.

This leads to the weakening of the precipitate strengthening. Before the turning point, the precipitate strengthening calculated by the spatial distribution is smaller than that of the classical model, as the dominant mechanism of precipitate strengthening is the shearing mechanism. After the turning point, as the effects of both shearing and Orowan bypassing mechanisms on individual precipitate are considered, the precipitation strengthening is greater than that of the classical model.

#### 3.3 Effect of the precipitate volume fraction

Figure 8 shows the relationship between the spatial distribution-dependent precipitate strengthening and the precipitate radius. The precipitate strengthening increases with the increasing precipitate volume fraction, and the precipitate radius required for the maximum precipitate strengthening increases. When the volume fraction of precipitates is large, more precipitates are needed to cut or bypass by dislocations in the slip plane.

The relationship between the spatial distribution-dependent precipitate strengthening and the precipitate volume fraction is analyzed in Fig. 9a. The precipitate strengthening

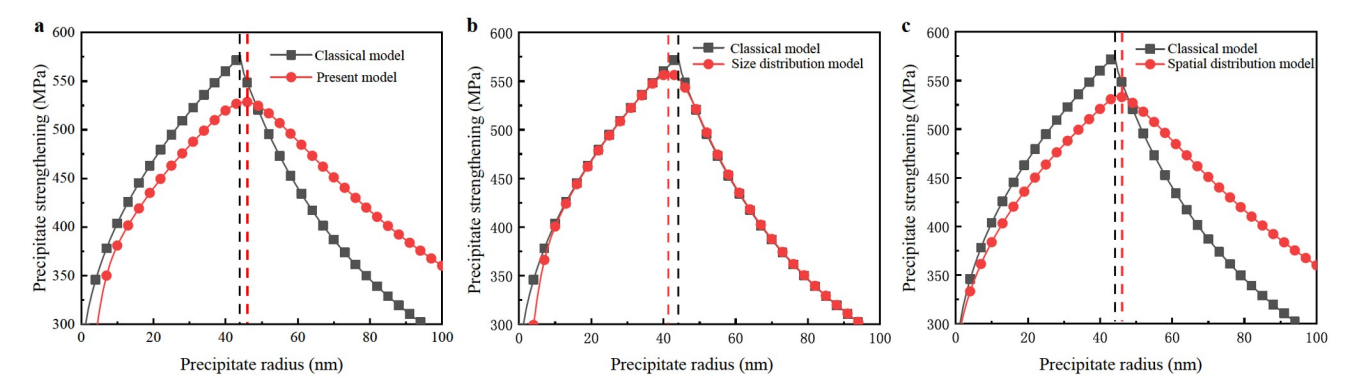
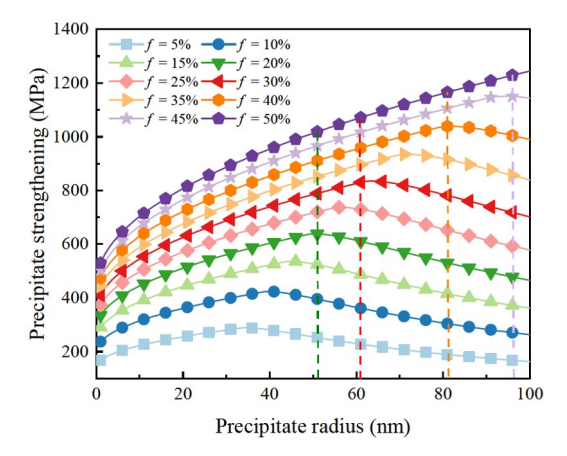


Figure 7 Curves of precipitate strengthening for the precipitate volume fraction of 14.9%. a Classical precipitate strengthening model and the present precipitate strengthening model; b classical precipitate strengthening model and the size distribution-dependent precipitate strengthening model; c classical precipitate strengthening model and the spatial distribution-dependent precipitate strengthening model.



**Figure 8** Spatial distribution-dependent precipitate strengthening versus precipitate radius for different precipitate volume fractions.

curves with different precipitate radii are staggered, suggesting that the precipitate strengthening is very sensitive to the precipitate radius. The precipitate strengthening increases with the increasing precipitate volume fraction, even though the precipitate radius is different.

As shown in Fig. 9b, when the radius meets  $r \le 30$  nm, the change rate of the precipitate strengthening to volume fraction decreases with the increased volume fraction, as the shearing mechanism dominates the precipitate strengthening (Fig. 9c). However, when the radius meets  $r \ge 60$  nm, the change rate begins to increase, due to that the dominant mechanism is the Orowan bypassing mechanism (Fig. 9c). With the increase of the volume fraction, the dominant precipitate mechanism changes to the shearing mechanism (Fig. 9c), leading to the decrease of change rate.

The relationship between the spatial distribution-dependent precipitate strengthening and precipitate radius is analyzed in Fig. 9d. The change rate of the spatial distribution-dependent precipitate strengthening to precipitate radii decreases with the increasing radius. The singularities represent that the dominant mechanism changes from the shearing mechanism to the Orowan bypassing mechanism

(Fig. 9d). By increasing the volume fraction, the range with a positive change rate can be extended to maximize the precipitate strengthening.

#### 3.4 Effect of the shear modulus difference

The modulus mismatch strengthening is the strengthening mechanism that can reflect the effect of material properties differences between precipitates and HEAs on the yield strength. Figure 10 shows the relationship between the shear modulus difference and modulus mismatch strengthening. The modulus mismatch strengthening enhances with the increase of the shear modulus difference, and radius as well as volume fraction. Here, the toughness loss caused by excessive shear modulus difference should be inestimable although modulus mismatch strengthening can increase with the increase of shear modulus difference. It is worth noting that a key issue associated with modeling strain hardening in the HEAs would be left in the future [43].

#### 4. Conclusion

A theoretical model of yield strength in the HEAs is developed by considering various strengthening mechanisms, including the solid solute strengthening, grain boundary strengthening, dislocation strengthening, and precipitate strengthening. In addition, a precipitate strengthening model is established in the HEAs, taking into account the size and spatial distribution. The developed model is in good agreement with the experiment and the accuracy is higher than the classical model, which verifies the reliability of the model.

From the analysis of the experimental data and the developed strengthening model, the following conclusions are obtained. The precipitate strengthening is the main contribution to yield strength in the FeCoCrNiTiAl and FeCoNiTiAl HEAs. The spatial distribution significantly

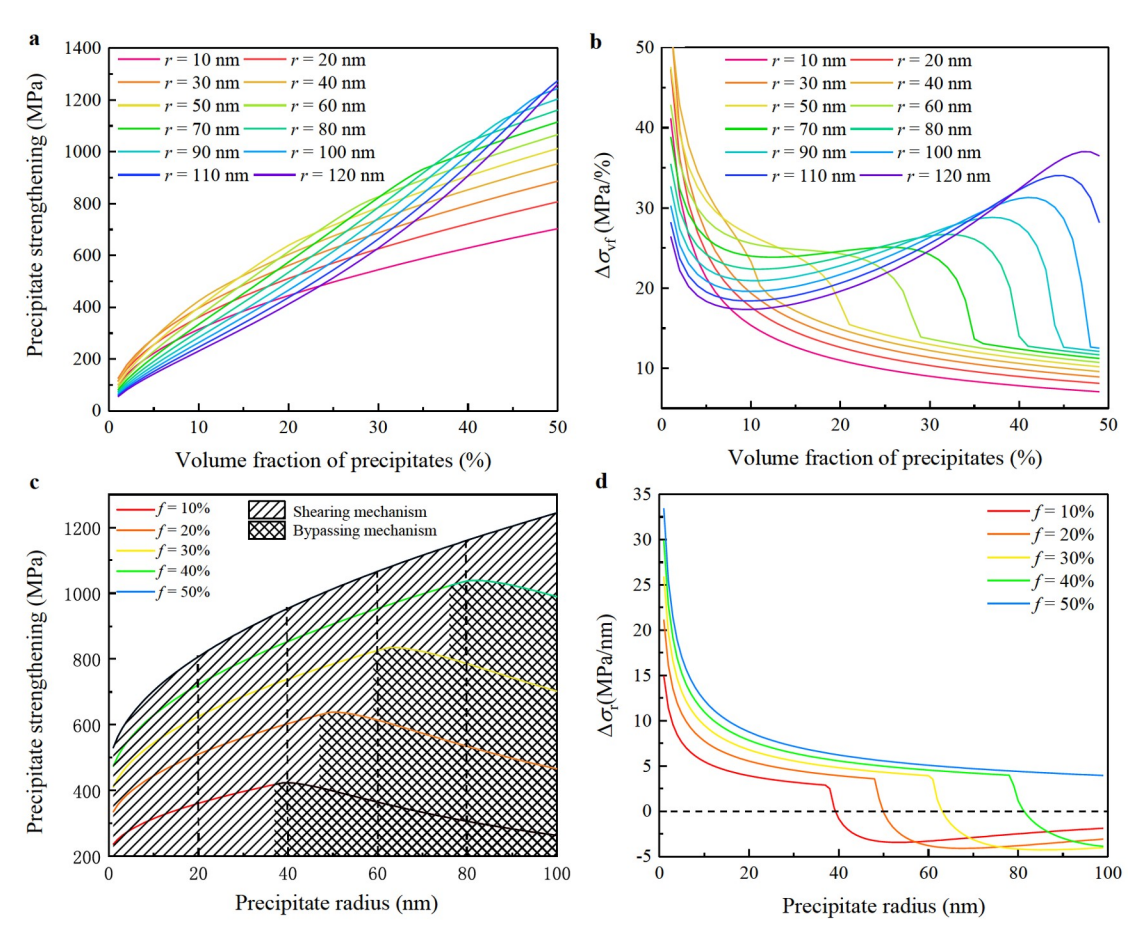


Figure 9 a Spatial distribution-dependent precipitate strengthening versus precipitate volume fraction for different precipitate radii; **b** change rate of the spatial distribution-dependent precipitate strengthening to precipitate volume fraction  $(\Delta \sigma_{vf})$  for different precipitate radii; **c** dominant mechanism regions in different spatial distribution-dependent precipitate strengthening curves; **d** change rate of the spatial distribution-dependent precipitate strengthening to precipitate radius  $(\Delta \sigma_v)$  for different precipitate volume fraction.

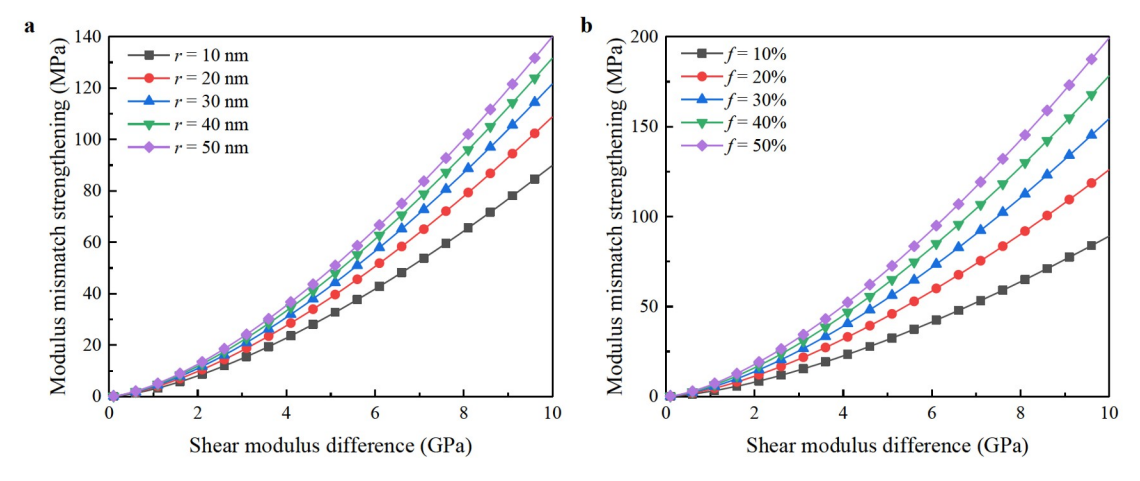


Figure 10 a Modulus mismatch strengthening versus shear modulus difference for different precipitate radii; b modulus mismatch strengthening versus shear modulus difference for different precipitate volume fractions.

influences the precipitate strengthening. However, the size distribution has little effect on the precipitate strengthening. In the relationship between the spatial distribution-dependent precipitate strengthening and the volume fraction, when the radius is smaller than the critical radius, the shearing

mechanism is triggered, resulting in the weakness of the precipitate strengthening. When the precipitate radius is larger than the critical radius, the dominant mechanism changes to the Orowan bypassing mechanism, leading to the enhancement of the precipitate strengthening.

Author contributions Siwei Ren established the theoretical model and data collection and wrote the first draft of the manuscript. Jia Li, Hui Feng, Peter K. Liaw, and Qihong Fang provided the idea and reviewed, revised, and edited the manuscript. Siwei Ren, Jia Li, and Hui Feng revised and edited the final version.

Acknowledgements This work was supported by the National Natural Science Foundation of China (Grant No. 12172123), the Natural Science Foundation of Hunan Province (Grant Nos. 2022JJ20001 and 2021JJ40032), the Science and Technology Innovation Program of Hunan Province (Grant No. 2022RC1200), and the Natural Science Foundation of Changsha City (Grant No. kq2202139), the National Science Foundation (Grant Nos. DMR-1611180 and 1809640), and the US Army Research Office (Grant Nos. W911NF-13-1-0438 and W911NF-19-2-0049).

- E. P. George, D. Raabe, and R. O. Ritchie, High-entropy alloys, Nat. Rev. Mater. 4, 515 (2019).
- Y. Zhang, T. T. Zuo, Z. Tang, M. C. Gao, K. A. Dahmen, P. K. Liaw, and Z. P. Lu, Microstructures and properties of high-entropy alloys, Prog. Mater. Sci. 61, 1 (2014).
- 3 J. Li, Y. Chen, Q. He, X. Xu, H. Wang, C. Jiang, B. Liu, Q. Fang, Y. Liu, Y. Yang, P. K. Liaw, and C. T. Liu, Heterogeneous lattice strain strengthening in severely distorted crystalline solids, Proc. Natl. Acad. Sci. USA 119, e2200607119 (2022).
- 4 B. Cantor, I. T. H. Chang, P. Knight, and A. J. B. Vincent, Microstructural development in equiatomic multicomponent alloys, Mater. Sci. Eng.-A 375-377, 213 (2004).
- 5 J. W. Yeh, S. K. Chen, S. J. Lin, J. Y. Gan, T. S. Chin, T. T. Shun, C. H. Tsau, and S. Y. Chang, Nanostructured high-entropy alloys with multiple principal elements: novel alloy design concepts and outcomes, Adv. Eng. Mater. 6, 299 (2004).
- 6 C. Lee, F. Maresca, R. Feng, Y. Chou, T. Ungar, M. Widom, K. An, J. D. Poplawsky, Y. C. Chou, P. K. Liaw, and W. A. Curtin, Strength can be controlled by edge dislocations in refractory high-entropy alloys, Nat. Commun. 12, 5474 (2021).
- 7 O. El-Atwani, N. Li, M. Li, A. Devaraj, J. K. S. Baldwin, M. M. Schneider, D. Sobieraj, J. S. Wróbel, D. Nguyen-Manh, S. A. Maloy, and E. Martinez, Outstanding radiation resistance of tungstenbased high-entropy alloys, Sci. Adv. 5, eaav2002 (2019).
- 8 Q. Pan, L. Zhang, R. Feng, Q. Lu, K. An, A. C. Chuang, J. D. Poplawsky, P. K. Liaw, and L. Lu, Gradient cell-structured high-entropy alloy with exceptional strength and ductility, Science 374, 984 (2021).
- 9 Y. Zhao, J. M. Park, J. Jang, and U. Ramamurty, Bimodality of incipient plastic strength in face-centered cubic high-entropy alloys, Acta Mater. 202, 124 (2021).
- B. Gludovatz, A. Hohenwarter, D. Catoor, E. H. Chang, E. P. George, and R. O. Ritchie, A fracture-resistant high-entropy alloy for cryogenic applications, Science 345, 1153 (2014).
- 11 Y. Wang, J. Wang, M. Lei, and Y. Yao, A crystal plasticity coupled damage constitutive model of high entropy alloys at high temperature, Acta Mech. Sin. 38, 122116 (2022).
- 12 H. Chen, X. Zhang, C. Liu, W. Xiong, M. Tan, and L. H. Dai, Theoretical analysis for self-sharpening penetration of tungsten high-entropy alloy into steel target with elevated impact velocities, Acta Mech. Sin. 37, 970 (2021).
- J. Y. He, H. Wang, Y. Wu, X. J. Liu, H. H. Mao, T. G. Nieh, and Z. P. Lu, Precipitation behavior and its effects on tensile properties of FeCoNiCr high-entropy alloys, Intermetallics 79, 41 (2016).
- J. Y. He, H. Wang, H. L. Huang, X. D. Xu, M. W. Chen, Y. Wu, X. J. Liu, T. G. Nieh, K. An, and Z. P. Lu, A precipitation-hardened high-entropy alloy with outstanding tensile properties, Acta Mater. 102, 187 (2016).

- 15 L. Guo, J. Gu, X. Gong, S. Ni, and M. Song, CALPHAD aided design of high entropy alloy to achieve high strength via precipitate strengthening, Sci. China Mater. 63, 288 (2020).
- 16 Y. L. Zhao, Y. R. Li, G. M. Yeli, J. H. Luan, S. F. Liu, W. T. Lin, D. Chen, X. J. Liu, J. J. Kai, C. T. Liu, and T. Yang, Anomalous precipitate-size-dependent ductility in multicomponent high-entropy alloys with dense nanoscale precipitates, Acta Mater. 223, 117480 (2022).
- 17 X. Wu, B. Wang, C. Rehm, H. He, M. Naeem, S. Lan, Z. Wu, and X. L. Wang, Ultra-small-angle neutron scattering study on temperature-dependent precipitate evolution in CoCrFeNiMo<sub>0.3</sub> high entropy alloy, Acta Mater. 222, 117446 (2022).
- 18 S. H. Shim, H. Pouraliakbar, B. J. Lee, Y. K. Kim, M. S. Rizi, and S. I. Hong, Strengthening and deformation behavior of as-cast CoCrCu<sub>1.5</sub> MnNi high entropy alloy with micro-/nanoscale precipitation, Mater. Sci. Eng.-A 853, 143729 (2022).
- 19 S. Y. Li, W. P. Wu, and M. X. Chen, An anisotropic micromechanics model for predicting the rafting direction in Ni-based single crystal superalloys, Acta Mech. Sin. 32, 135 (2016).
- 20 D. N. Seidman, E. A. Marquis, and D. C. Dunand, Precipitation strengthening at ambient and elevated temperatures of heat-treatable Al(Sc) alloys, Acta Mater. 50, 4021 (2002).
- 21 J. F. Nie, and B. C. Muddle, Characterisation of strengthening precipitate phases in a Mg-Y-Nd alloy, Acta Mater. 48, 1691 (2000).
- 22 M. P. Petkov, J. Hu, E. Tarleton, and A. C. F. Cocks, Comparison of self-consistent and crystal plasticity FE approaches for modelling the high-temperature deformation of 316H austenitic stainless steel, Int. J. Solids Struct. 171, 54 (2019).
- 23 S. Peng, Y. Wei, and H. Gao, Nanoscale precipitates as sustainable dislocation sources for enhanced ductility and high strength, Proc. Natl. Acad. Sci. USA 117, 5204 (2020).
- 24 E. Nembach, Particle Strengthening of Metals and Alloys (Wiley, New York, 1997).
- 25 M. F. Ashby, Physics of Strength and Plasticity (MIT Press, Cambridge, 1969).
- 26 T. Gladman, The Physical Metallurgy of Microalloyed Steels (CRC Press, Boca Raton, 1996).
- 27 H. Wen, T. D. Topping, D. Isheim, D. N. Seidman, and E. J. Lavernia, Strengthening mechanisms in a high-strength bulk nanostructured Cu-Zn-Al alloy processed via cryomilling and spark plasma sintering, Acta Mater. 61, 2769 (2013).
- 28 K. Ma, H. Wen, T. Hu, T. D. Topping, D. Isheim, D. N. Seidman, E. J. Lavernia, and J. M. Schoenung, Mechanical behavior and strengthening mechanisms in ultrafine grain precipitation-strengthened aluminum alloy, Acta Mater. 62, 141 (2014).
- 29 C. Booth-Morrison, D. C. Dunand, and D. N. Seidman, Coarsening resistance at 400 °C of precipitation-strengthened Al-Zr-Sc-Er alloys, Acta Mater. 59, 7029 (2011).
- 30 X. Liu, P. Liu, W. Zhang, Q. Hu, Q. Chen, N. Gao, Z. Tu, Z. Fan, and G. Liu, Microstructure and mechanical properties of face-centered-cubic-based Cr-free equiatomic high-entropy alloys, Adv. Eng. Mater. 23, 2000848 (2021).
- 31 Y. Mu, L. He, S. Deng, Y. Jia, Y. Jia, G. Wang, Q. Zhai, P. K. Liaw, and C. T. Liu, A high-entropy alloy with dislocation-precipitate skeleton for ultrastrength and ductility, Acta Mater. 232, 117975 (2022).
- 32 V. Nandal, R. Sarvesha, S. S. Singh, E. W. Huang, Y. J. Chang, A. C. Yeh, S. Neelakantan, and J. Jain, Influence of pre-deformation on the precipitation characteristics of aged non-equiatomic Co<sub>1.5</sub>CrFeNi<sub>1.5</sub> high entropy alloys with Ti and Al additions, J. Alloys Compd. 855,

- 157521 (2021).
- 33 L. Li, Q. Fang, J. Li, B. Liu, Y. Liu, and P. K. Liaw, Lattice-distortion dependent yield strength in high entropy alloys, Mater. Sci. Eng.-A 784, 139323 (2020).
- 34 E. O. Hall, The deformation and ageing of mild steel: III discussion of results, Proc. Phys. Soc. B **64**, 747 (1951).
- 35 W. H. Liu, Y. Wu, J. Y. He, T. G. Nieh, and Z. P. Lu, Grain growth and the Hall-Petch relationship in a high-entropy FeCrNiCoMn alloy, Scripta Mater. 68, 526 (2013).
- 36 N. N. Vinh, Study on dislocation cell structure, dislocation density-fatigue property relationship of a structural steel, J. Sci. Tech. Civ. Eng. 16, 29 (2022).
- 37 J. E. Bailey, and P. B. Hirsch, The dislocation distribution, flow stress, and stored energy in cold-worked polycrystalline silver, Philos. Mag. 5, 485 (1960).
- 38 S. Ren, L. Li, Q. Fang, and J. Li, Modeling and analysis of yielding and strain hardening in metastable high-entropy alloys, Physica Status Solidi (b) 258, 2100247 (2021).

- 39 J. Peng, L. Li, F. Li, B. Liu, S. Zherebtsov, Q. Fang, J. Li, N. Stepanov, Y. Liu, F. Liu, and P. K. Liaw, The predicted rate-dependent deformation behaviour and multistage strain hardening in a model heterostructured body-centered cubic high entropy alloy, Int. J. Plast. 145, 103073 (2021).
- 40 J. Y. He, C. Zhu, D. Q. Zhou, W. H. Liu, T. G. Nieh, and Z. P. Lu, Steady state flow of the FeCoNiCrMn high entropy alloy at elevated temperatures, Intermetallics 55, 9 (2014).
- 41 T. M. Pollock, and A. S. Argon, Creep resistance of CMSX-3 nickel base superalloy single crystals, Acta Metall. Mater. 40, 1 (1992).
- 42 C. Xu, W. J. Dai, Y. Chen, Z. X. Qi, G. Zheng, Y. D. Cao, J. P. Zhang, C. C. Bu, and G. Chen, Control of dislocation density maximizing precipitation strengthening effect, J. Mater. Sci. Tech. 127, 133 (2022).
- 43 Q. Fang, W. Lu, Y. Chen, H. Feng, P. K. Liaw, and J. Li, Hierarchical multiscale crystal plasticity framework for plasticity and strain hardening of multi-principal element alloys, J. Mech. Phys. Solids 169, 105067 (2022).

### 沉淀强化高熵合金屈服强度及本构模型研究

任思危, 李甲, 冯慧, Peter K. Liaw, 方棋洪

**摘要** 沉淀强化高熵合金表现出优异的强度和延展性. 然而, 由于现有的模型忽略了高熵合金中复杂化学元素、析出相尺寸分布和空间分布在内的关键作用, 使之无法准确预测高熵合金中固溶强化和沉淀强化对屈服强度的贡献. 此外, 还缺乏统一的强度模型来分析高熵合金中的屈服强度. 本文建立了考虑尺寸分布和空间分布的沉淀强化模型, 与现有模型相比, 该模型具有更高的精度. 结果表明, 沉淀强化在屈服强度中起主要贡献作用. 此外, 空间分布对沉淀强化的影响比析出相尺寸分布的影响更显著. 该模型为确定高熵合金的沉淀强化和屈服强度提供了理论框架, 并为设计高强度高熵合金提供指导.